ACS NANO

www.acsnano.org

Two-Step Patterning of Scalable All-Inorganic Halide Perovskite Arrays

Chung-Kuan Lin,[∇] Qiuchen Zhao,[∇] Ye Zhang, Stefano Cestellos-Blanco, Qiao Kong, Minliang Lai, Joohoon Kang, and Peidong Yang*

Cite This: https://dx.doi.org/10.1021/acsnano.9b09685 Read Online

ACCESS | Metrics & More | Article Recommendations | Supporting Information

ABSTRACT: Halide perovskites have many important optoelectronic properties, including high emission efficiency, high absorption coefficients, color purity, and tunable emission wavelength, which makes these materials promising for optoelectronic applications. However, the inability to precisely control large-scale patterned growth of halide perovskites limits their potential toward various device applications. Here, we report a patterning method for the growth of a cesium lead halide perovskite single crystal array. Our approach consists of two steps: (1) cesium halide salt arrays patterning and (2) chemical vapor transport process to convert salt arrays into single crystal perovskite arrays. Characterizations including energy-dispersive X-ray spectroscopy and photoluminescence have been employed to confirm the chemical compositions and the optical properties of the as-synthesized perovskite arrays. This patterning method enables the patterning of single crystal cesium lead halide perovskite arrays with tunable spacing (from 2 to 20 μm) and crystal size (from 200 nm to 1.2 μm) in high production yield (almost every pixel in the array is successfully grown with converted perovskite crystals). Our large-scale patterning method renders a platform for the study of fundamental properties and opportunities for perovskite-based optoelectronic applications.

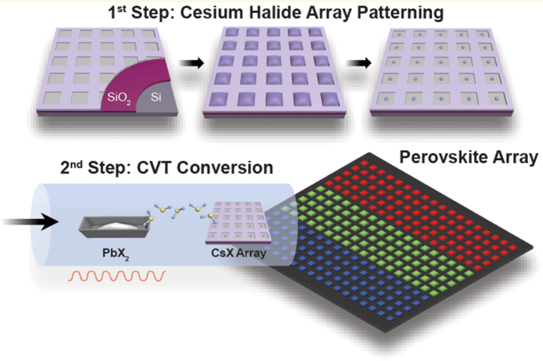

KEYWORDS: *halide perovskite, patterning, crystal growth, large-scale array, chemical vapor transport, perovskite optoelectronics*

Lead halide perovskites, corner-shared octahedral structures with typical formula of $APbX_3$ ($A = Cs^+$, $CH_3NH_3^+$, $X = Cl^-$, Br^-, I^-), have excited the community with many important optoelectronic properties, such as high emission efficiency,[1] high absorption coefficients,[2] color purity, and tunable emission wavelength.[3] These properties have made perovskite a strong candidate for optoelectronic applications, such as light-emitting diodes (LEDs),[4] photodetectors,[5−9] and lasers.[10,11] The ability to create a periodic array structure is of central importance to developing various optoelectronic applications. Although some efforts has been put to develop a dry transfer technique for hybrid perovskites,[12] the chemical instability in various solvents and ambient conditions still makes current nanofabrication techniques difficult to be applied directly to perovskites.[13,14]

To date, diverse efforts have been developed to produce perovskite arrays, including direct and indirect patterning methods.[15] The main advantage of direct patterning is that it allows for high controllability. A typical method for direct patterning is inkjet printing,[16,17] which creates spatially controlled polycrystalline or single crystal perovskite arrays with careful optimization of precursor amounts.[16,18−21] Another direct patterning approach consists of employing a focused ion beam (FIB) or laser beam to etch and transform perovskite thin films into intended patterns.[22−24] Other common approaches for direct patterning are micro/nanoimprint methods,[25−27] which utilize molds (typically made by PDMS, or other templates) with designed patterns. Perovskite precursors (usually gel or solution) are first deposited on a substrate,[26,28] and the mold is placed with a certain pressure on the top. The periodic pattern underneath is created after evaporation of solvents. These direct patterning methods can reach microscale precision and can be achieved by programmable arbitrary patterns with inkjet printing.

Indirect patterning, on the other hand, provides process scalability. In this method, various pretreatments are employed to obtain patterns on substrates, followed by

Received: December 9, 2019
Accepted: February 14, 2020
Published: February 14, 2020

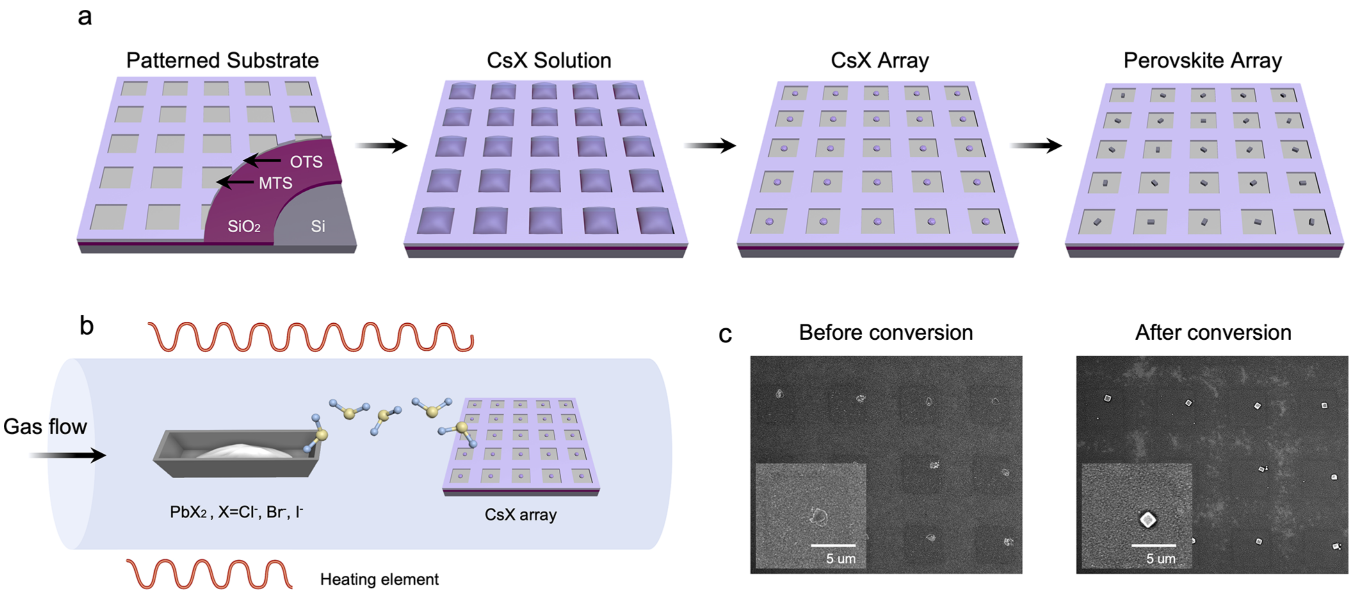

Figure 1. Schematic illustration, experimental setup, and typical results of patterning process. (a) A schematic elucidating the process from creating prepatterned substrate, growth of CsX arrays, and conversion of perovskite arrays. (b) A schematic showing the quartz tube and furnace heating element. The boat with PbX_2 is placed upstream, and CsX arrays placed downstream. A nitrogen gas flow was maintained during the CVT process to transport PbX_2. (c) SEM image of as-prepared CsX arrays (left) and perovskite arrays after CVT conversion (right).

selective growth of periodic perovskite structures.[29−31] Periodic two-dimensional (2D) material arrays, such as graphene or boron nitride,[29,30] or hydrophilic/hydrophobic patterns by surface modification methods are widely used to grow perovskite crystal arrays.[31] In 2015, Duan and co-workers designed a method, using an octadecyltrichlorosilane (OTS) monolayer pattern on a Si/SiO_2 substrate, to define hydrophilic areas on a hydrophobic surface, followed by a seed growth to create PbI_2 arrays.[31] The PbI_2 arrays were converted into $(CH_3NH_3)PbI_3$ by a gas−solid process with methylammonium iodide vapor. This bottom-up method not only preserved the crystallinity of perovskites but also facilitated the large-scale patterned growth.

However, hybrid perovskite optoelectronics are still facing the challenges of stability under ambient conditions,[13,14] and their all-inorganic counterpart could therefore be a candidate to overcome these difficulties due to better thermal, oxygen, and moisture stability.[32−34] Simply adopting the patterning method from the hybrid halide perovskite case to the all-inorganic version may not be applicable due to the lower vapor pressure of inorganic halide compared with the methylammonium halide. Here, we report a two-step patterning method to produce single crystal all-inorganic perovskite arrays. This method exploits the melting temperature difference between CsX and PbX_2 (X = Cl^-, Br^-, I^-) and soft ionic bonding nature of perovskite structure. Cesium halide (higher melting point) arrays were grown on a prepatterned hydrophobic/hydrophilic surface, and then a chemical vapor transport (CVT) process is used to convert the CsX into $CsPbX_3$ perovskite arrays. This method can be generalized and extended to all three halides (Cl^-, Br^-, I^-) that are typically used for emission color tunability of the halide perovskite family. A series of characterization methods were carried out to further confirm the composition of the as-grown perovskite arrays. Our method allows us to grow scalable single crystal inorganic halide perovskite arrays with controllable crystal size (from 200 nm to 1 μm) and spacing (from 2 to 20 μm) in high production yield (every pixel in the array is successfully grown with a converted perovskite crystals). Furthermore, this approach renders a platform to develop perovskite optoelectronics, such as high-quality LED displays and high-sensitive photodetectors. Moreover, our scheme has enabled the patterned growth of perovskite arrays on wafer-scale Si substrates, creating a pathway for integrating perovskite emitters with Si photonics.

RESULTS AND DISCUSSION

Perovskite crystal arrays were successfully grown in a two-step patterning process that involved the growth of CsX arrays and conversion to perovskite crystals (Figure 1a). A patterned substrate with wettability contrast was designed by photolithography and a subsequent surface modification process (more details are shown in SI method). Cesium halide aqueous solution was flowed through the patterned substrate (Figure 1a, step 2), and droplets of the CsX solution were confined in hydrophilic squares. The CsX preferentially nucleated inside the square area (Figure 1a, step 3) after evaporation of the solvent. These CsX were each converted into $CsPbX_3$ perovskite crystals through a CVT conversion process (Figure 1b), by using a PbX_2 solid precursor with the same halide. Figure 1c shows the scanning electron microscopy (SEM) image before (left, CsX salt) and after (right, perovskite crystal) conversion in an individual window. This demonstrated that the polycrystalline salt can be converted into a cubic-shaped perovskite, and in most of the windows, a single nucleus formed.

Variations in surface modifications in the patterning process resulted in differing perovskite crystal features. A typical hydrophobic surface modification agent,[31] OTS ($CH_3(CH_2)_{17}SiCl_3$), was employed in our patterning process to form a hydrophobic self-assembled monolayers (SAMs) grid. When OTS reacted with hydroxyl groups on the SiO_2 surface, a Si−O bond formed, and the surface was modified

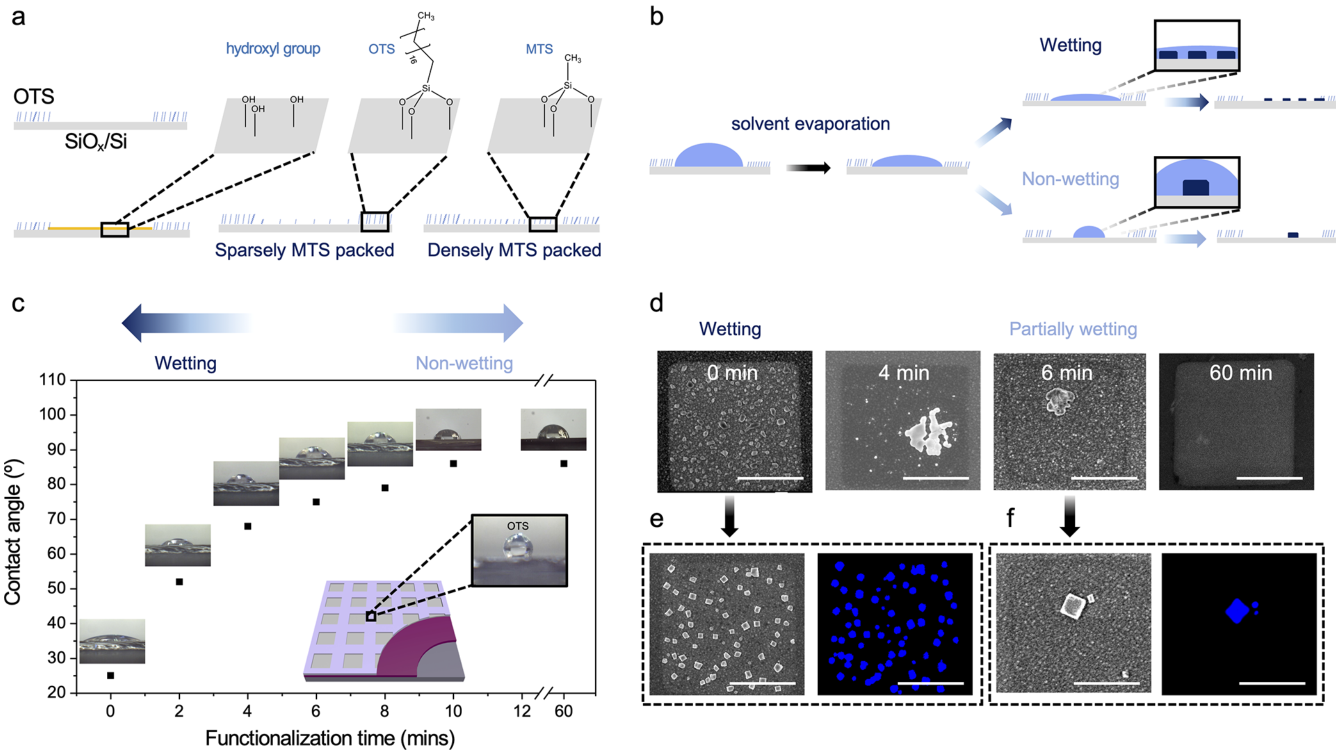

Figure 2. Schematics of patterning method and results. (a) Schematics of different surface conditions. Top row: Surface with OH group, OTS, and MTS respectively. Bottom row, left: Hydroxylation surface. Middle: Sparsely MTS treated surface. Right: Densely MTS treated surface. (b) Schematics elucidating interaction between droplet and surface in wetting (top row) and nonwetting (bottom row) cases. (c) Contact angle changes with different MTS functionalization time. Inset: Water droplet on OTS modified Si/SiO$_2$ substrate. (d) Morphology of CsCl with different MTS functionalization time. From left to right: 0 min, 4 min, 6 min, and 60 min (no nucleation). Scale bar: 5 *μ*m. (e,f) SEM and PL images of converted CsPbCl$_3$ on wetting (e) and partially wetting (f) substrates. Scale bar: 5 *μ*m.

with long chain alkyl groups ($C_{18}H_{37}^-$, shown in Figure 2a, top row middle case). The wettability contrast between hydrophilic square area (SiO_2) and hydrophobic grid (OTS) would confine solution droplets when CsX aqueous solution flowed though. During the dewetting process, patterned substrate with suitable wettability conditions plays an important role in obtaining CsX arrays.[16,35−38] We hypothesized that the dewetting dynamics, including droplet confinement, evaporation, and evolution of the three-phase contact line, would depend on the wettability between surface and droplets.[38] This process was essentially a competition between pinning forces (because of solvent and substrate surface interaction) and depinning forces (deviation of the droplet profile from equilibrium due to evaporation). During evaporation of the solvent, the contact line was anchored on the wetting substrate[39] (Figure 2b, top row), but receded on nonwetting substrates.[40] (Figure 2b, bottom row) As the solvent evaporated, and when the concentration of the solution reached a supersaturated critical point, CsX precipitated and nucleated on the surface. For the wetting substrate (as shown in Figure 2b top row), the nucleation took place over the whole square due to anchored contact line and resulted in multiple nucleation sites. On the contrary, when the substrate was nonwetting, the contact line of the droplet on the surface (see Figure 2b bottom row) receded significantly at the critical concentration, and the salt precipitated in a localized area.

To further control wettability of the inner-square area, we employed methyltrichlorosilane (MTS) as a surface modification agent and systematically studied the relationship between surface wettability and CsX nucleation. The SiO_2 surface was first treated with NaOH, then immersed in dilute MTS-hexane solution (1:25,000) for various amounts of time (4, 6, and 60 min). This procedure allowed us to control wettability contrast in the inner square area. The original OTS grid was not affected by NaOH or MTS treatment (shown in Figure S1). NaOH activated the bare SiO_2 surface with hydroxyl groups to make it hydrophilic due to hydrogen-bonding interaction between substrate and solvent. When MTS reacted with the NaOH-modified substrate, the Si−O bond formed and the surface was functionalized by methyl groups. MTS has a shorter alkyl chain (Figure 2a) compared to OTS. The surface with methyl groups was more hydrophobic than the surface with hydroxyl groups, but was less hydrophobic compared with OTS-modified surface.

The MTS coverage increased with the immersion time as indicated by the contact angle measurement (Figure 2c), used to quantify the interaction between substrate and droplets. Varying the immersion time from 0 to 10 min resulted in the change of contact angle from 30° to 86°, demonstrating that the wettability of the inner-square area can be effectively controlled. With a short immersion time, inner-square area was sparsely covered by MTS (Figure 2a, bottom row, middle case), and the contact angle is relatively small, indicating a stronger droplet-substrate interaction. On the contrary, with longer immersion time, the surface was densely covered by MTS (as shown in Figure 2a bottom row, right-hand-side case), and the surface was more hydrophobic and resulted in weaker interaction with the droplet. However, after a 60 min

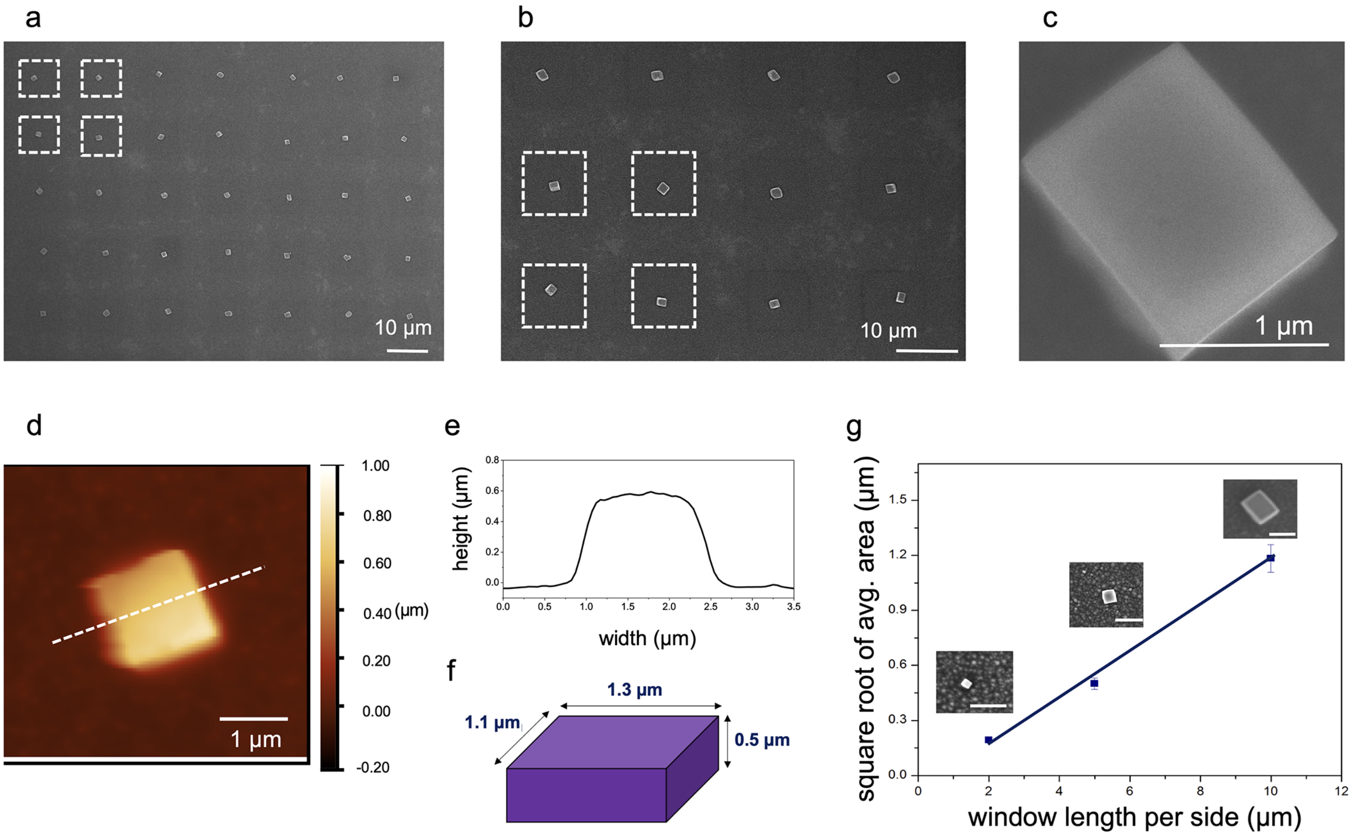

Figure 3. Morphology of $CsPbCl_3$ arrays. (a−c) SEM images of as-grown perovskite arrays. (d) AFM image and (e) height profile of a single $CsPbCl_3$ plate. (f) Schematic of reconstructed $CsPbCl_3$ plate. (g) Dependence of window length to square root of $CsPbCl_3$ area. Inset: SEM image of $CsPbCl_3$ with different sizes and geometry. Scale bar: 1 *μ*m.

immersion time in MTS, the contact angle remained almost constant.

The SEM was used to further examine the morphology of CsX nucleation sites under various wettability conditions. The SEM images of the as-patterned crystal morphology shown in Figure 2d correspond to the substrate immersed in MTS for 0 (NaOH treatment only), 4, 6, and 60 min, respectively, and CsCl was selected as a representative for discussion. In the case of high wettability, with fully wetting substrate (NaOH treatment only, no MTS treatment, with the contact angle around 30°), the CsX tended to form multiple nucleation sites. With moderate wettability, partially wetting substrate (immersed in MTS solution from 4 to 6 min, with the contact angle around 65° and 75°, respectively), the CsCl with polycrystalline morphology, localized distribution and dendritic structure was obtained. When the substrate was too nonwetting (after 60 min MTS treatment, with the contact angle around 86°), no salt nucleation was found since the wettability contrast between the inner-square area and OTS grid was too low to confine the droplet (both were too hydrophobic). These experimental results were consistent with our previous hypothesis that dewetting dynamics impacted the CsX nucleation. We determined that MTS treatment with 6 min immersion was the ideal condition to obtain the CsX nucleus in a localized area for conversion into single crystal perovskite phase, for only one crystal per square area (Figure 2f). More quantitative analysis of the nucleation process can be found in SI2.

The as-prepared CsX samples were then converted into halide perovskite crystals *via* chemical vapor transportation (CVT). SEM images in Figure 2e,f show the perovskite ($CsPbCl_3$) formed from a wetting substrate and partially wetting substrate, respectively. In both samples, every salt nucleus was converted into a cubic crystal. The chemical composition of the as-converted crystal was confirmed by photoluminescence (PL) mapping, which showed a strong emission wavelength at 423 nm (Figure 2e,f), and agrees with the reported emission wavelength of $CsPbCl_3$.[3] The wetting substrate resulted in multinuclei perovskite cubes with relatively small size and distributed randomly across the entire square area. On the contrary, partially wetting substrate mainly had one large $CsPbCl_3$ cube inside. It is worth mentioning that this conversion process began as a polycrystalline salt structure and resulted in a single crystal perovskite. A melting-nucleation mechanism according to the phase diagram can explain this process. In this CVT process, PbX_2 (placed upstream) was continuously transported and reacted with CsX arrays (placed downstream), gradually changing the CsX:PbX_2 ratio. As shown on the CsBr-$PbBr_2$ phase diagram (see Figure S2), with the amount of CsBr fixed, as the $PbBr_2$ ratio in the system gradually increased, the melting point of the CsBr and $PbBr_2$ mixture decreased. We hypothesize that the decreasing melting point could lead to a premelting process under our deposition temperature (400 °C). After the system passed the first eutectic point, the solid-phase $CsPbBr_3$ gradually precipitated from the solution and slowly crystallized into single crystalline perovskite structure, while the ratio between CsX and PbX_2 is 1:1. This process is further discussed in SI3.

https://dx.doi.org/10.1021/acsnano.9b09685
ACS Nano XXXX, XXX, XXX−XXX

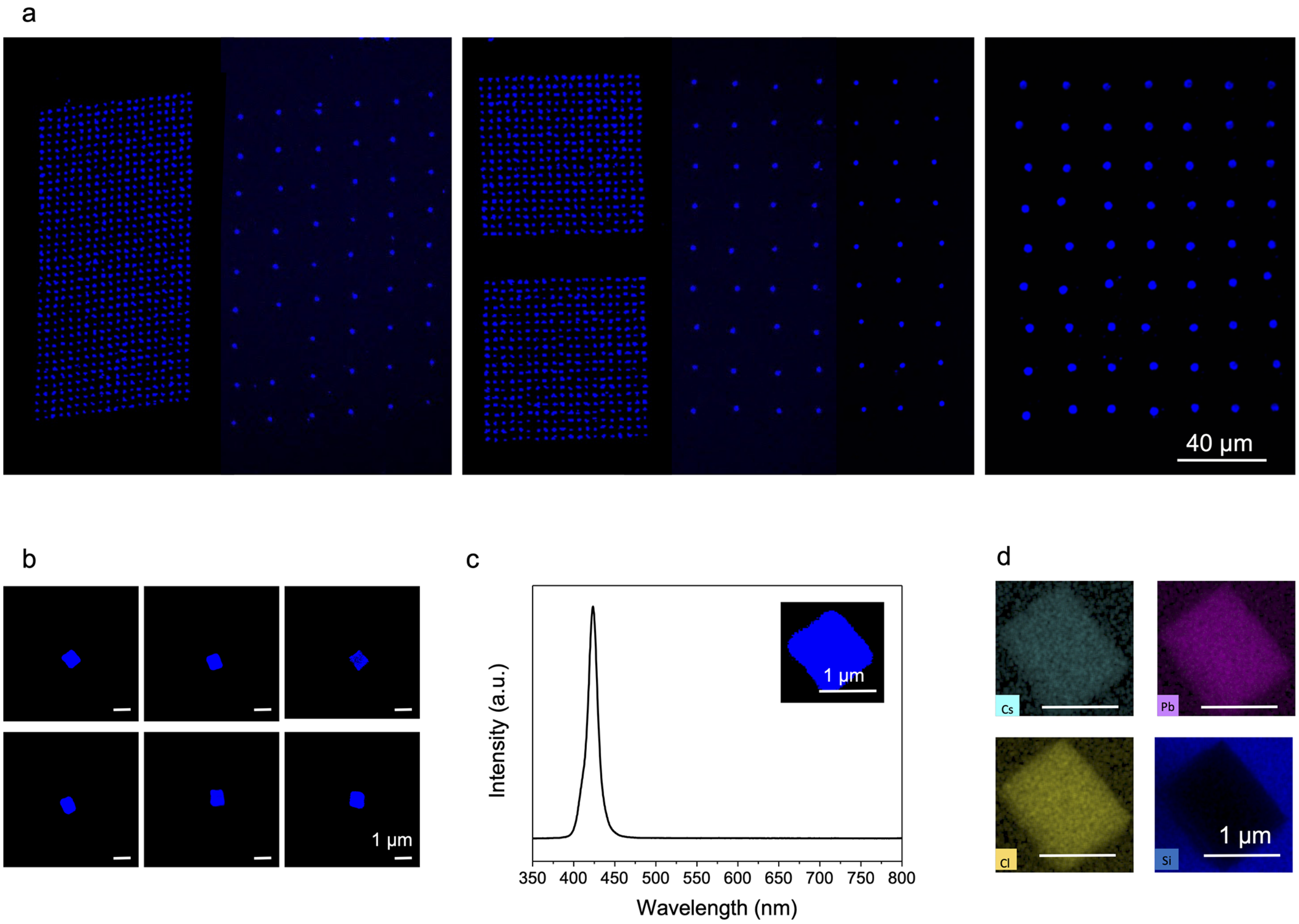

Figure 4. Composition of $CsPbCl_3$ arrays. (a) Panorama PL images of as-grown perovskite arrays. (b) PL images of individual crystal taken by confocal microscope. (c) PL spectrum of the grown $CsPbCl_3$ array. (d) SEM-EDS mapping of Cs, Pb, Cl, and Si.

A series of systematical characterization methods have been carried out to confirm the composition, morphology, and optical properties of as-synthesized perovskite arrays; $CsPbCl_3$ was also selected as a representative for discussion. Figure 3a–c shows SEM images of $CsPbCl_3$ crystal arrays and the zoomed-in image in a square. Each square is 10 μm × 10 μm with a distance of 10 μm apart from each other. From the SEM image, one can observe the contrast difference between the OTS layer (outside the square) and the inner-square area. The square areas in SEM images were marked by a white-dashed line. $CsPbCl_3$ crystal thickness was measured by atomic force microscopy (AFM), as shown in Figure 3d,e, at a height of around 0.5 μm. The length and width of the crystal can also be measured *via* SEM, which is around 1.3 and 1.1 μm, respectively. Figure 3f shows a schematic of reconstructed $CsPbCl_3$ plate, which has comparable lengths in three dimensions. Furthermore, the size of $CsPbCl_3$ crystals was controlled by varying the size of the hydrophilic square area. By changing the length of the square area (2, 5, and 10 μm, respectively), the $CsPbCl_3$ crystal width can be tuned from ~200 nm to 1.2 μm (Figure 3g inset from left to right). A linear relationship was observed between average length of the perovskites plate and length of the square area (Figure 3g); this indicates that the area of the square determines the volume of CsCl solution droplet confined and further defines the final size of the perovskite crystal.

Large-area arrays were patterned with different sizes and geometries, and the PL panorama of all arrays are shown in Figure 4a. To further confirm the uniformity of our as-grown crystals, we sampled over 20 spectra from individual crystal and performed a statistical analysis on line widths and emission peaks. The average line width was 69.7 meV with a standard deviation of 4.27 meV, and the emission peak from all individual crystals centered at 423 ± 1 nm. Figure 4b is PL images of some of the individual crystals we sampled over for statistics. The PL spectrum was used to confirm its composition (Figure 4c), which agrees with reported emission of $CsPbCl_3$ crystals.[5] The PL emission from arrays also aligns with our confocal PL measurement (Figure 4c), which further confirmed uniformity of the arrays. Figure 4c inset shows a confocal PL mapping of the individual plate with uniform emission, indicating a highly crystalline quality of the grown perovskite crystals. The chemical composition and distribution of corresponding elements in $CsPbCl_3$ plates were confirmed by energy-dispersive X-ray spectroscopy (EDS), showing that Cs, Pb, and Cl were uniformly distributed in the crystal (Figure 4d), with the ratio of 1:0.96:2.63, which is roughly around 1:1:3 (see SI4, Table 1).

Our two-step synthesis approach can also be generalized and extended to other halides. Figure 5 shows $CsPbBr_3$ and $CsPbI_3$ arrays that converted from cesium bromide and cesium iodide, respectively. SEM images of the perovskite crystals arrays (left), a zoomed-in morphology (inset), and a

https://dx.doi.org/10.1021/acsnano.9b09685
ACS Nano XXXX, XXX, XXX−XXX

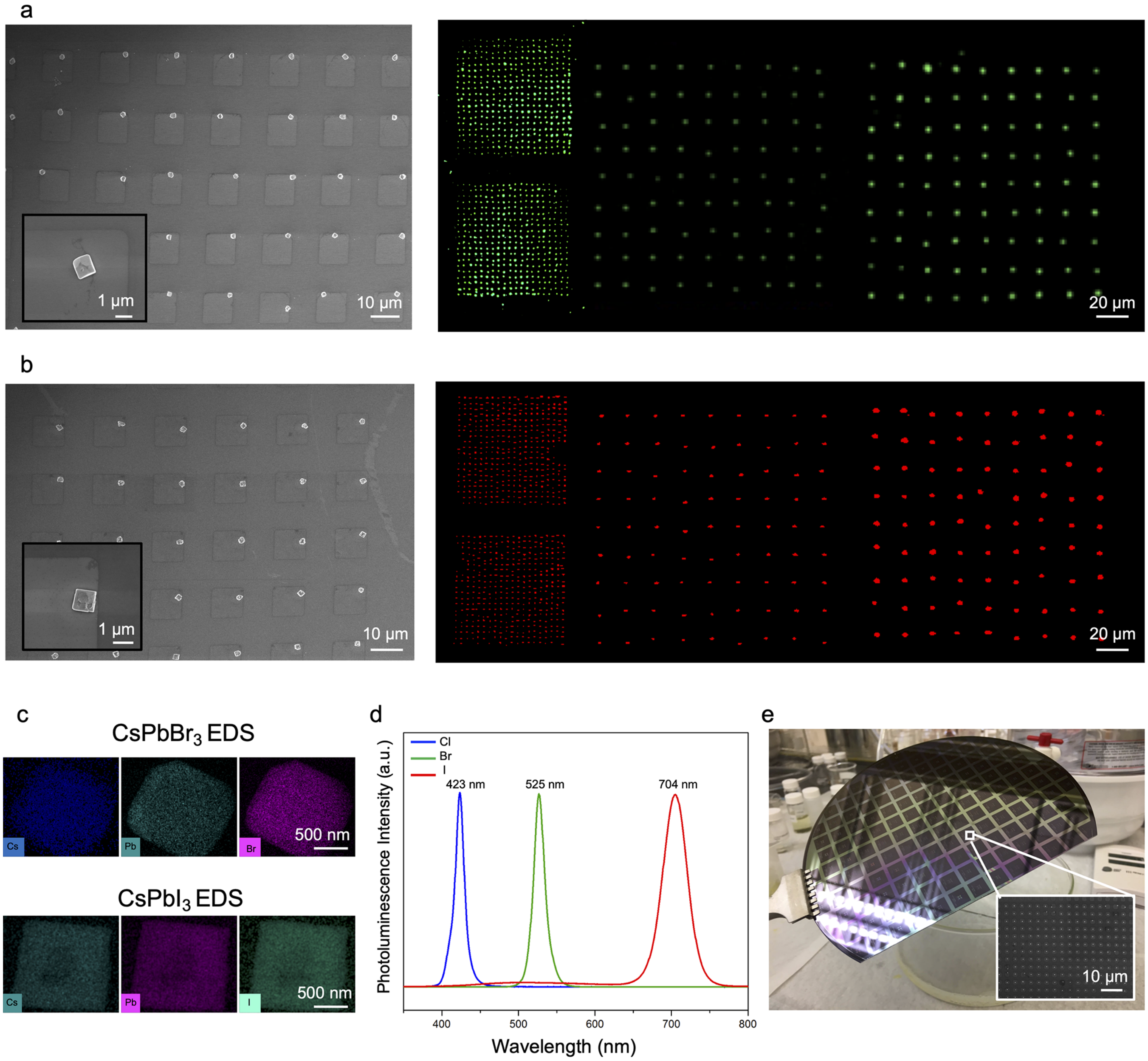

Figure 5. Characterizations of CsPbBr$_3$ and CsPbI$_3$ arrays. (a) Left: SEM image of CsPbBr$_3$ arrays. Scale bar: 10 μm. Inset: Zoomed-in image of a single CsPbBr$_3$ plate. Scale bar: 1 μm. Right: Panorama PL image of CsPbBr$_3$ arrays. Scale bar: 20 μm (b) Left: SEM image of CsPbI$_3$ array. Scale bar: 10 μm. Inset: Zoomed-in image of a single CsPbI$_3$ plate. Scale bar: 1 μm. Right: Panorama PL image of CsPbI$_3$ arrays. Scale bar: 20 μm. (c) Top: SEM-EDS mapping of the CsPbBr$_3$ crystal. Bottom: SEM-EDS mapping of the CsPbI$_3$ crystal. Scale bar: 500 nm. (d) PL spectra of CsPbCl$_3$ (blue), CsPbBr$_3$ (green), and CsPbI$_3$ (red) respectively. (e) Photo of a 6 in. wafer. Entire wafer was dip-coated into CsCl solution, and CsCl salt arrays can be created all at once.

corresponding PL image panorama (right) are shown in Figure 5a,b. An EDS mapping (Figure 5c) shows that all of the Cs, Pb, and halide elements are uniformly distributed in the crystal, with a ratio roughly around 1:1:3 as well (more details shown in SI4, Table 2−3). PL spectrum of the array centered at 525 ± 1 and 704 ± 1 nm, respectively (Figure 5d), aligns with previous reports and further confirms the chemical composition of the crystals.[4,41] CsPbBr$_3$ arrays were converted with a slightly lower temperature compared to CsPbCl$_3$, due to the lower melting points of both CsBr and PbBr$_2$. It is also worth mentioning that due to structural differences between PbI$_2$ and the other two lead halides, the conversion strategy needs to be slightly modified. As a layered structure, PbI$_2$ crystals can easily nucleate into hexagonal flakes at lower energy nucleation sites. When the same method was used to grow CsPbI$_3$ arrays, instead of obtaining pure CsPbI$_3$ arrays, hexagonal PbI$_2$ flakes tended to form and grow from CsI, which served as a competing nucleation site (see Figure S4). Therefore, in this case, the growth approach was slightly modified. CsI array was placed on top of the ceramics boat instead of being placed downstream. When PbI$_2$ precursors were heated to targeted temperature, the PbI$_2$ vapor directly reacted with CsI array and yielded highly crystalline, high-T phase CsPbI$_3$ plates. Furthermore, we scale up our patterning method to a 6 in. Si/SiO$_2$ wafer, as shown in Figure 5e. By dipping the prepatterned wafer into CsX solution several times and taking it out, CsX periodic arrays can be readily produced all at once. This demonstrates that our patterning method is robust and scalable, creating a method for industrial-scale production for optoelectronic applications.

CONCLUSION

In conclusion, we have developed a two-step, bottom-up patterning method to grow single crystal metal halide perovskite arrays with tunable size and spacing in high yield. Polycrystalline CsX arrays are patterned on a hydrophilic/hydrophobic silicon substrate. Our work also provides scientific insight on the influence of surface wettability to crystal morphology during the dewetting process. The patterned CsX arrays are converted into single crystal perovskite arrays through a subsequent CVT process. Our method can be extended to different halides to realize all-inorganic metal halide perovskite arrays in three colors and has the capability of state-of-art scalable device fabrications, such as high spatial controllability and scalability. The ability to pattern all-inorganic perovskite arrays provides a platform for fundamental studies and for future optoelectronic applications.

METHODS

Preparation of Patterned Substrate. A typical commercial photolithography exposure machine was used to pattern the photoresist (i-line Fujifilm OIR 906-12) squares on the Si/SiO_2 substrate. After the photoresist squares were patterned, the substrate was immersed in a mixture of OTS hexane solvent (1:250 v/v, Sigma-Aldrich, 99%) for 1 h to assemble the OTS monolayer. The substrate was then washed with acetone to dissolve photoresist and treated with NaOH (2 mol/L) for 10 s. Thereafter, the substrate was immersed in dilute methyltrichlorosilane (MTS) hexane solution (MTS, 1:25000 v/v, Sigma-Aldrich, 99%) for a required time to create a submonolayer MTS on newly exposed SiO_2 surface.

Preparation of CsX Salt Array. As-prepared CsX (CsX powder from Sigma-Aldrich, 99.99%) aqueous solution (concentration around 0.6 M) was heated at 80 °C and flowed through the tilted patterned Si/SiO_2 substrate. CsX salt nucleated in each hydrophilic region as the solution flowed through.

Chemical Vapor Transport Conversion. The $CsPbX_3$ ($X = Cl^-, Br^-$) perovskite nanoplates were converted by a chemical vapor transport (CVT) method in a tube furnace (TF55035A). A ceramic boat loaded with precursors of PbX_2 (X = Cl, Br; 99.999% Sigma-Aldrich) was placed at the heating center of a 1 in.-diameter quartz tube. The as-prepared CsX array on a Si/SiO_2 substrate was placed downstream, which was 12 cm (for Cl case) or 14 cm (for Br case) away from the tube center. A carrier gas of high-purity N_2 (99.998%) with a flow rate of 200 sccm was used to purge the tube system in order to eliminate oxygen and moisture in the tube and also to transport the PbX_2 to react with CsX arrays. The center temperature was set to ramp from room temperature to 400 °C with a heating rate of 50 °C/min, maintained at 400 °C for 40 min, and later cooled down to room temperature in 4 h.

The $CsPbI_3$ perovskite nanoplates were also converted by the same CVT system. A ceramic boat loaded with precursors of PbI_2 (powder, 99.999% Sigma-Aldrich) was put at the heating center of a 1 in.-diameter quartz tube. CsI salt array was placed directly on the top of the ceramics boat. The system was heated to 300 °C in 10 min, maintained for 40 min, and cooled down to room temperature in 4 h.

Material Characterization. SEM images were acquired using a JEOL JSM-6340F field emission scanning electron microscope. PL spectra were measured using a 375 nm excitation from a laser diode, with emission collected on a Nikon A1 microscope connected with a multimode fiber coupled to a liquid-nitrogen-cooled Si CCD. Optical PL images were acquired *via* an Olympus IX71 inverted microscope coupled to a Zeiss AxioCam MRc5 camera. The PL panorama image was taken with a laser scanning confocal microscope, Zeiss LSM710. The thickness of nanoplates was measured using an atomic force microscope (MFP-3D Asylum Research, Oxford Instruments) equipped with an acoustic isolation chamber (AEK 2002) and a silicon tip (AC240TS-R3, Asylum Research, Oxford Instruments).

ASSOCIATED CONTENT

Supporting Information

The Supporting Information is available free of charge at https://pubs.acs.org/doi/10.1021/acsnano.9b09685.

> Experimental details and additional characterizations. Figures show additional contact angle measurements, contact angle schematics, SEM images of PbI_2/CsI conversion growth, $CsBr-PbBr_2$ phase diagram and XRD. Tables show SEM-EDX data on $CsPbX_3$. (PDF)

AUTHOR INFORMATION

Corresponding Author

Peidong Yang – *Department of Chemistry and Department of Materials Science and Engineering, University of California Berkeley, Berkeley, California 94720, United States; Materials Sciences Division, Lawrence Berkeley National Laboratory, Berkeley, California 94720, United States; Kavli Energy NanoScience Institute, Berkeley, California 94720, United States;* orcid.org/0000-0003-4799-1684; Email: p_yang@berkeley.edu

Authors

Chung-Kuan Lin – *Department of Chemistry, University of California Berkeley, Berkeley, California 94720, United States; Materials Sciences Division, Lawrence Berkeley National Laboratory, Berkeley, California 94720, United States;* orcid.org/0000-0001-9193-2345

Qiuchen Zhao – *Department of Chemistry, University of California Berkeley, Berkeley, California 94720, United States*

Ye Zhang – *Department of Chemistry, University of California Berkeley, Berkeley, California 94720, United States; Materials Sciences Division, Lawrence Berkeley National Laboratory, Berkeley, California 94720, United States*

Stefano Cestellos-Blanco – *Department of Materials Science and Engineering, University of California Berkeley, Berkeley, California 94720, United States*

Qiao Kong – *Department of Chemistry, University of California Berkeley, Berkeley, California 94720, United States*

Minliang Lai – *Department of Chemistry, University of California Berkeley, Berkeley, California 94720, United States*

Joohoon Kang – *Department of Chemistry, University of California Berkeley, Berkeley, California 94720, United States; Kavli Energy NanoScience Institute, Berkeley, California 94720, United States; Center for NanoMedicine, Institute for Basic Science (IBS); Y-IBS Institute, Yonsei University, Seoul 03722, Korea; School of Advanced Materials Science and Engineering, Sungkyunkwan University (SKKU), Suwon 16419, Korea;* orcid.org/0000-0002-6578-2547

Complete contact information is available at: https://pubs.acs.org/10.1021/acsnano.9b09685

Author Contributions

$^{\nabla}$These authors contributed equally to this work. C.K.L., Q.Z., and P.Y. designed the experiments and wrote the paper. C.K.L. and Q.Z. grew and converted the $CsPbX_3$ array. C.K.L.

carried out optical spectroscopy measurements and confocal images. Q.Z. designed and performed the surface modification and contact angle measurements. Y.Z. performed the AFM measurements. S.C. conducted the photolithography. C.K.L. and Q.K. performed SEM and EDX measurements. P.Y. supervised the project. All authors discussed the results and commented on the manuscript.

Notes

The authors declare no competing financial interest.

ACKNOWLEDGMENTS

We thank Rachel Chan for helpful discussions on the work and manuscript preparation and Chris Jackson, Zhenni Lin, and Mengyu Gao for fruitful discussion. We thank Jianbo Jin for the help on XRD measurements. This work was supported by the US Department of Energy, Office of Science, Office of Basic Energy Sciences, Materials Sciences and Engineering Division, under contract DE-AC02-05CH11231 within the Physical Chemistry of Inorganic Nanostructures Program (KC3103). Confocal laser scanning microscopic study was conducted at the College of Natural Resources Biological Imaging Facility, supported in part by the National Institutes of Health S10 Program under award 1S10RR026866-01. SEM-EDX performed at Molecular Foundry was supported by the Office of Science, Office of Basic Energy Science, of the U.S. Department of Energy. Y.Z., M.L., and Q.K. acknowledge a fellowship from Suzhou Industrial Park. S.C.-B. thanks the Philomathia Foundation for support. J.K. acknowledges IBS Global Postdoctoral Fellowship (IBS-R026-D1). C.K.L. gratefully acknowledges Taiwan MOE scholarship.

REFERENCES

(1) Kim, Y.; Yassitepe, E.; Voznyy, O.; Comin, R.; Walters, G.; Gong, X.; Kanjanaboos, P.; Nogueira, A. F.; Sargent, E. H. Efficient Luminescence from Perovskite Quantum Dot Solids. *ACS Appl. Mater. Interfaces* **2015**, *7*, 25007−25013.

(2) Park, N.-G. Perovskite Solar Cells: An Emerging Photovoltaic Technology. *Mater. Today* **2015**, *18*, 65−72.

(3) Protesescu, L.; Yakunin, S.; Bodnarchuk, M. I.; Krieg, F.; Caputo, R.; Hendon, C. H.; Yang, R. X.; Walsh, A.; Kovalenko, M. V. Nanocrystals of Cesium Lead Halide Perovskites ($CsPbX_3$, X = Cl, Br, and I): Novel Optoelectronic Materials Showing Bright Emission with Wide Color Gamut. *Nano Lett.* **2015**, *15*, 3692−3696.

(4) Xing, J.; Zhao, Y.; Askerka, M.; Quan, L. N.; Gong, X.; Zhao, W.; Zhao, J.; Tan, H.; Long, G.; Gao, L.; Yang, Z.; Voznyy, O.; Tang, J.; Lu, Z. H.; Xiong, Q.; Sargent, E. H. Color-Stable Highly Luminescent Sky-Blue Perovskite Light-Emitting Diodes. *Nat. Commun.* **2018**, *9*, 3541.

(5) Wang, H.; Kim, D. H. Perovskite-Based Photodetectors: Materials and Devices. *Chem. Soc. Rev.* **2017**, *46*, 5204−5236.

(6) Tsai, W.-L.; Chen, C.-Y.; Wen, Y.-T.; Yang, L.; Cheng, Y.-L.; Lin, H.-W. Band Tunable Microcavity Perovskite Artificial Human Photoreceptors. *Adv. Mater.* **2019**, *31*, 1900231.

(7) Wu, J.; Chen, J.; Zhang, Y.; Xu, Z.; Zhao, L.; Liu, T.; Luo, D.; Yang, W.; Chen, K.; Hu, Q.; Ye, F.; Wu, P.; Zhu, R.; Gong, Q. Pinhole-Free Hybrid Perovskite Film with Arbitrarily-Shaped Micro-Patterns for Functional Optoelectronic Devices. *Nano Lett.* **2017**, *17*, 3563−3569.

(8) Choi, C.; Choi, M. K.; Liu, S.; Kim, M. S.; Park, O. K.; Im, C.; Kim, J.; Qin, X.; Lee, G. J.; Cho, K. W.; Kim, M.; Joh, E.; Lee, J.; Son, D.; Kwon, S.-H.; Jeon, N. L.; Song, Y. M.; Lu, N.; Kim, D.-H. Human Eye-Inspired Soft Optoelectronic Device Using High-Density MoS_2-Graphene Curved Image Sensor Array. *Nat. Commun.* **2017**, *8*, 1664.

(9) Feng, J.; Gong, C.; Gao, H.; Wen, W.; Gong, Y.; Jiang, X.; Zhang, B.; Wu, Y.; Wu, Y.; Fu, H.; Jiang, L.; Zhang, X. Single-Crystalline Layered Metal-Halide Perovskite Nanowires for Ultrasensitive Photodetectors. *Nat. Electron.* **2018**, *1*, 404−410.

(10) Wang, Y.-C.; Li, H.; Hong, Y.-H.; Hong, K.-B.; Chen, F.-C.; Hsu, C.-H.; Lee, R.-K.; Conti, C.; Kao, T. S.; Lu, T.-C. Flexible Organometal−Halide Perovskite Lasers for Speckle Reduction in Imaging Projection. *ACS Nano* **2019**, *13*, 5421−5429.

(11) Eaton, S. W.; Lai, M.; Gibson, N. A.; Wong, A. B.; Dou, L.; Ma, J.; Wang, L.-W.; Leone, S. R.; Yang, P. Lasing in Robust Cesium Lead Halide Perovskite Nanowires. *Proc. Natl. Acad. Sci. U. S. A.* **2016**, *113*, 1993−1998.

(12) Leng, K.; Abdelwahab, I.; Verzhbitskiy, I.; Telychko, M.; Chu, L.; Fu, W.; Chi, X.; Guo, N.; Chen, Z.; Chen, Z.; et al. Molecularly Thin Two-Dimensional Hybrid Perovskites with Tunable Optoelectronic Properties Due to Reversible Surface Relaxation. *Nat. Mater.* **2018**, *17*, 908−914.

(13) Misra, R. K.; Aharon, S.; Li, B.; Mogilyansky, D.; Visoly-Fisher, I.; Etgar, L.; Katz, E. A. Temperature- and Component-Dependent Degradation of Perovskite Photovoltaic Materials under Concentrated Sunlight. *J. Phys. Chem. Lett.* **2015**, *6*, 326−330.

(14) Berhe, T. A.; Su, W.-N.; Chen, C.-H.; Pan, C.-J.; Cheng, J.-H.; Chen, H.-M.; Tsai, M.-C.; Chen, L.-Y.; Dubale, A. A.; Hwang, B.-J. Organometal Halide Perovskite Solar Cells: Degradation and Stability. *Energy Environ. Sci.* **2016**, *9*, 323−356.

(15) Yang, X.; Wu, J.; Liu, T.; Zhu, R. Patterned Perovskites for Optoelectronic Applications. *Small Methods* **2018**, *2*, 1800110.

(16) Gu, Z.; Wang, K.; Li, H.; Gao, M.; Li, L.; Kuang, M.; Zhao, Y. S.; Li, M.; Song, Y. Direct-Writing Multifunctional Perovskite Single Crystal Arrays by Inkjet Printing. *Small* **2017**, *13*, 1603217.

(17) Zhou, N.; Bekenstein, Y.; Eisler, C. N.; Zhang, D.; Schwartzberg, A. M.; Yang, P.; Alivisatos, A. P.; Lewis, J. A. Perovskite Nanowire−Block Copolymer Composites with Digitally Programmable Polarization Anisotropy. *Sci. Adv.* **2019**, *5*, eaav8141.

(18) Liu, Y.; Li, F.; Qiu, L.; Yang, K.; Li, Q.; Zheng, X.; Hu, H.; Guo, T.; Wu, C.; Kim, T. W. Fluorescent Microarrays of *In Situ* Crystallized Perovskite Nanocomposites Fabricated for Patterned Applications by Using Inkjet Printing. *ACS Nano* **2019**, *13*, 2042−2049.

(19) Zhao, C.; Li, H.; Wang, Y.; Li, K.; Hou, J.; Ma, Y.; Li, M.; Song, Y. A General Layer-by-Layer Printing Method for Scalable High-Resolution Full-Color Flexible Luminescent Patterns. *Adv. Opt. Mater.* **2019**, *7*, 1900127.

(20) Zhu, M.; Duan, Y.; Liu, N.; Li, H.; Li, J.; Du, P.; Tan, Z.; Niu, G.; Gao, L.; Huang, Y.; Yin, Z.; Tang, J. Electrohydrodynamically Printed High-Resolution Full-Color Hybrid Perovskites. *Adv. Funct. Mater.* **2019**, *29*, 1903294.

(21) Wong, Y. C.; Wu, W. B.; Wang, T.; Ng, J. A.; Khoo, K. H.; Wu, J.; Tan, Z. K. Color Patterning of Luminescent Perovskites *via* Light-Mediated Halide Exchange with Haloalkanes. *Adv. Mater.* **2019**, 1901247.

(22) Alias, M. S.; Dursun, I.; Shi, D.; Saidaminov, M. I.; Diallo, E. M.; Priante, D.; Ng, T. K.; Bakr, O. M.; Ooi, B. S. Focused-Ion Beam Patterning of Organolead Trihalide Perovskite for Subwavelength Grating Nanophotonic Applications. *J. Vac. Sci. Technol., B: Nanotechnol. Microelectron.: Mater., Process., Meas., Phenom.* **2015**, 33, 051207.

(23) Chou, S. S.; Swartzentruber, B. S.; Janish, M. T.; Meyer, K. C.; Biedermann, L. B.; Okur, S.; Burckel, D. B.; Carter, C. B.; Kaehr, B. Laser Direct Write Synthesis of Lead Halide Perovskites. *J. Phys. Chem. Lett.* **2016**, *7*, 3736−3741.

(24) Alias, M. S.; Yang, Y.; Ng, T. K.; Dursun, I.; Shi, D.; Saidaminov, M. I.; Priante, D.; Bakr, O. M.; Ooi, B. S. Enhanced Etching, Surface Damage Recovery, and Submicron Patterning of Hybrid Perovskites Using a Chemically Gas-Assisted Focused-Ion Beam for Subwavelength Grating Photonic Applications. *J. Phys. Chem. Lett.* **2016**, *7*, 137−142.

(25) Wang, H.; Haroldson, R.; Balachandran, B.; Zakhidov, A.; Sohal, S.; Chan, J. Y.; Zakhidov, A.; Hu, W. Nanoimprinted

Perovskite Nanograting Photodetector with Improved Efficiency. *ACS Nano* **2016**, *10*, 10921−10928.

(26) Jeong, B.; Hwang, I.; Cho, S. H.; Kim, E. H.; Cha, S.; Lee, J.; Kang, H. S.; Cho, S. M.; Choi, H.; Park, C. Solvent-Assisted Gel Printing for Micropatterning Thin Organic−Inorganic Hybrid Perovskite Films. *ACS Nano* **2016**, *10*, 9026−9035.

(27) Feng, J.; Yan, X.; Zhang, Y.; Wang, X.; Wu, Y.; Su, B.; Fu, H.; Jiang, L. "Liquid Knife" to Fabricate Patterning Single-Crystalline Perovskite Microplates toward High-Performance Laser Arrays. *Adv. Mater.* **2016**, *28*, 3732−3741.

(28) Kim, W.; Jung, M. S.; Lee, S.; Choi, Y. J.; Kim, J. K.; Chai, S. U.; Kim, W.; Choi, D.-G.; Ahn, H.; Cho, J. H.; Choi, D.; Shin, H.; Kim, D.; Park, J. H. Oriented Grains with Preferred Low-Angle Grain Boundaries in Halide Perovskite Films by Pressure-Induced Crystallization. *Adv. Energy Mater.* **2018**, *8*, 1702369.

(29) Niu, L.; Liu, X.; Cong, C.; Wu, C.; Wu, D.; Chang, T. R.; Wang, H.; Zeng, Q.; Zhou, J.; Wang, X.; Fu, W.; Yu, P.; Fu, Q.; Najmaei, S.; Zhang, Z.; Yakobson, B. I.; Tay, B. K.; Zhou, W.; Jeng, H. T.; Lin, H.; Sum, T. C.; Jin, C.; He, H.; Yu, T.; Liu, Z. Controlled Synthesis of Organic/Inorganic van der Waals Solid for Tunable Light−Matter Interactions. *Adv. Mater.* **2015**, *27*, 7800−7808.

(30) Wu, C. Y.; Wang, Z.; Liang, L.; Gui, T.; Zhong, W.; Du, R. C.; Xie, C.; Wang, L.; Luo, L. B. Graphene-Assisted Growth of Patterned Perovskite Films for Sensitive Light Detector and Optical Image Sensor Application. *Small* **2019**, *15*, 1900730.

(31) Wang, G.; Li, D.; Cheng, H.-C.; Li, Y.; Chen, C.-Y.; Yin, A.; Zhao, Z.; Lin, Z.; Wu, H.; He, Q.; et al. Wafer-Scale Growth of Large Arrays of Perovskite Microplate Crystals for Functional Electronics and Optoelectronics. *Sci. Adv.* **2015**, *1*, e1500613.

(32) Huang, J.; Lai, M.; Lin, J.; Yang, P. Rich Chemistry in Inorganic Halide Perovskite Nanostructures. *Adv. Mater.* **2018**, *30*, 1802856.

(33) Saliba, M.; Matsui, T.; Domanski, K.; Seo, J.-Y.; Ummadisingu, A.; Zakeeruddin, S. M.; Correa-Baena, J.-P.; Tress, W. R.; Abate, A.; Hagfeldt, A.; Grätzel, M. Incorporation of Rubidium Cations into Perovskite Solar Cells Improves Photovoltaic Performance. *Science* **2016**, *354*, 206−209.

(34) McMeekin, D. P.; Sadoughi, G.; Rehman, W.; Eperon, G. E.; Saliba, M.; Hörantner, M. T.; Haghighirad, A.; Sakai, N.; Korte, L.; Rech, B.; Johnston, M. B.; Herz, L. M.; Snaith, H. J. A Mixed-Cation Lead Mixed-Halide Perovskite Absorber for Tandem Solar Cells. *Science* **2016**, *351*, 151−155.

(35) Qin, D.; Xia, Y.; Xu, B.; Yang, H.; Zhu, C.; Whitesides, G. M. J. A. M. Fabrication of Ordered Two-Dimensional Arrays of Micro- and Nanoparticles Using Patterned Self-Assembled Monolayers as Templates. *Adv. Mater.* **1999**, *11*, 1433−1437.

(36) Rio, E.; Daerr, A.; Lequeux, F.; Limat, L. Moving Contact Lines of a Colloidal Suspension in the Presence of Drying. *Langmuir* **2006**, *22*, 3186−3191.

(37) Cheng, W.; Park, N.; Walter, M. T.; Hartman, M. R.; Luo, D. Nanopatterning Self-Assembled Nanoparticle Superlattices by Moulding Microdroplets. *Nat. Nanotechnol.* **2008**, *3*, 682−690.

(38) Orejon, D.; Sefiane, K.; Shanahan, M. E. Stick−Slip of Evaporating Droplets: Substrate Hydrophobicity and Nanoparticle Concentration. *Langmuir* **2011**, *27*, 12834−12843.

(39) Bourges-Monnier, C.; Shanahan, M. J. L. Influence of Evaporation on Contact Angle. *Langmuir* **1995**, *11*, 2820−2829.

(40) McHale, G.; Rowan, S. M.; Newton, M. I.; Banerjee, M. K. Evaporation and the Wetting of a Low-Energy Solid Surface. *J. Phys. Chem. B* **1998**, *102*, 1964−1967.

(41) Lai, M.; Kong, Q.; Bischak, C. G.; Yu, Y.; Dou, L.; Eaton, S. W.; Ginsberg, N. S.; Yang, P. Structural, Optical, and Electrical Properties of Phase-Controlled Cesium Lead Iodide Nanowires. *Nano Res.* **2017**, *10*, 1107−1114.

https://dx.doi.org/10.1021/acsnano.9b09685